



HAL
open science

LiDAR and SCADA Data Processing for Interacting Wind Turbine Wakes with Comparison to Analytical Wake Models

Amr Hegazy, Frédéric Blondel, Marie Cathelain, Sandrine Aubrun

► **To cite this version:**

Amr Hegazy, Frédéric Blondel, Marie Cathelain, Sandrine Aubrun. LiDAR and SCADA Data Processing for Interacting Wind Turbine Wakes with Comparison to Analytical Wake Models. *Renewable Energy*, 2022, 181, pp.457-471. 10.1016/j.renene.2021.09.019 . hal-03462159

HAL Id: hal-03462159

<https://ifp.hal.science/hal-03462159>

Submitted on 1 Dec 2021

HAL is a multi-disciplinary open access archive for the deposit and dissemination of scientific research documents, whether they are published or not. The documents may come from teaching and research institutions in France or abroad, or from public or private research centers.

L'archive ouverte pluridisciplinaire **HAL**, est destinée au dépôt et à la diffusion de documents scientifiques de niveau recherche, publiés ou non, émanant des établissements d'enseignement et de recherche français ou étrangers, des laboratoires publics ou privés.

LiDAR and SCADA data processing for interacting wind turbine wakes with comparison to analytical wake models

Amr Hegazy ^{a,1}, Frédéric Blondel ^b, Marie Cathelain ^b, Sandrine Aubrun ^{a,*}

^a École Centrale de Nantes, LHEEA, 1 rue de la Noë, 44321, Nantes, France

^b IFP Energies nouvelles, 1&4 avenue du Bois Préau, 92862 Rueil-Malmaison, France

* Corresponding author: Email address: sandrine.aubrun@ec-nantes.fr (Sandrine Aubrun)

Abstract: This study is a follow up on a previous one carried out within the frame of the French project SMARTEOLE, during which, a ground-based scanning LiDAR measurement campaign was conducted in the onshore wind farm of Sole du Moulin Vieux. That previous study focused on the wakes of two wind turbines that experienced different degrees of interaction depending on the incoming wind direction, through the processing of LiDAR measurements. The measurement duration (7 months) ensured the statistical convergence of the ensemble-averaged flow fields obtained after holding a categorisation process based on the wind speed at hub height, wind direction, and atmospheric stability, where only near-neutral stability conditions were considered. The present study focuses on integrating the operational data of the wind turbines through SCADA processing to complement the LiDAR wake field observations and to be used as an input for analytical wake models. First, the correlation between the atmospheric stability, deduced from MERRA-2 dataset, and the free-stream turbulence intensity, measured by the wind turbines' anemometers, is studied for different wind speed ranges. It is observed that the turbulence intensity tends towards a consistent value as the atmospheric stability approaches near-neutral stability conditions, giving confidence into the applied strategy of data categorisation based on MERRA-2 outputs. The influence of the degree of wake interaction on the wake added turbulence, the velocity and power deficits between both turbines is assessed. Clear trends between the wake added turbulence and both the velocity and power deficits are detected. Consequently, two fitting laws are proposed. Then, different analytical wake models and wake superposition methods are fed with the operational data deduced from the processed SCADA data, and are used for predicting the evolution of the velocity deficit within the wake. Some statistical metrics are used for error quantification of the different engineering wake models compared to the scanning LiDAR measurements, used as reference, and Blondel and Cathelain produces the closest results to the field measurements.

Keywords: Wind energy; Atmospheric boundary layer; Wind turbine wake; Wake interactions; Wake models; Wake superposition

¹ Present address: Delft Centre for Systems and Control, Delft University of Technology, Mekelweg 2, 2628 CD, Delft, The Netherlands

39
40
41
42
43
44
45
46
47
48
49
50
51
52
53
54
55
56
57
58
59
60
61
62
63
64
65
66
67
68
69
70
71
72
73
74
75
76
77
78
79
80
81
82
83
84
85
86
87
88
89

1. Introduction

The urgent need for designing large wind farm arrays requires a deep understanding of the wind turbine (WT) wakes, as their quantification and modelling are challenging, not only for the scientific community, but also for wind farm developers. When a WT operates within the wake of another, a reduction in its incoming wind speed occurs, which causes power losses that can reach 20% of the power generated from the undisturbed ones [1–3]. Furthermore, WTs experience fatigue loads due to the increased turbulence intensity within the wakes, leading to the reduction of their lifetime. Therefore, any improvements in the understanding and characterisation of WT wakes would reduce the uncertainties in the power losses [4], lead to an increase the power production, hence, increase the economic viability of wind energy [5].

When air flows over a WT, it is affected by its presence both upstream and downstream [5,6]. Consequently, the area surrounding a WT is divided into an upstream region called *induction zone* reaching up to a distance of $2D_r$, D_r being the rotor diameter, whereas the downstream one is called *wake region*. In the induction zone, wind speed is progressively reduced upstream of the turbine [5,7,8]. The wake is composed of two sub-regions; the near-wake region that lies directly downstream the turbine with a length of $2 - 4D_r$ [5], and the far-wake region that starts after the near-wake region. The location and extent of the transition between near- and far-wake regions are not fully identified and depend on the environmental conditions, WT operational points, etc.

There are several approaches to study the flow over WTs. They include analytical models [5, 9–15], computational fluid dynamics (CFD) [16–20], wind tunnel experiments [21–23] and field experiments [24–26]. Analytical modelling presents a simple approach that requires low computational cost and is thus preferred in industry for wind farm design. CFD on the other hand, is a more sophisticated and expensive approach, yet gives more physical insight. Wind tunnel experiments provide valuable information on the flow structure of WT wakes in homogeneous and boundary layer flows, and very useful datasets for the validation of analytical and CFD models. However, it is always difficult to resemble the real process in the lab due to the applied trade-offs (e.g., full similarity issues). Field measurements provide the real-life insights, but they often lack statistical convergence because of the continuous changes in the atmospheric conditions and terrain properties, which affects the wake characteristics significantly [1]. Therefore, long term field observations are essential for proper wake characterisation [1,27,28]. It is also difficult to have high spatial precision measurements.

Field measurements used to be collected using anemometers mounted either on meteorological masts or on the turbines themselves to measure WT wakes. Nowadays, scanning wind Light Detection And Ranging (LiDAR) is used more often [1,5], which helps overcome the drawbacks of using anemometers; including poor space resolution and limited wind direction [1].

Regarding analytical wake modelling, there are several models that are simple and computationally inexpensive, yet superior in capturing the physics when compared to empirical models (i.e., obtained by data fitting) such as Zhang *et al.* [29], Iungo and Porté-Agel [30], and Aitken *et al.* [31]. This is due to the fact that these analytical wake models such as Jensen [9], Ainslie [10], Larsen [11], Frandsen *et al.* [12], Bastankhah and Porté-Agel [13], Qian and Ishihara [14], and Blondel and Cathelain [15] are derived from flow governing equations; either mass conservation equation only or mass and momentum conservation equations together [5]. The models that attracted attention the most (Jensen [9], Frandsen *et al.* [12], Bastankhah and Porté-Agel [13]), and a new promising one (Blondel and Cathelain [15]), are used in this study.

Jensen [9] assumed a top-hat shape for the wake velocity deficit profile which was based on solving the mass conservation equation only [5,9,13,15,32]. Duc *et al.* [33] proposed a tuning procedure to improve the accuracy of Jensen wake model based on locally updating the wake decay constant at each WT depending on the turbulence intensity measured by the nacelle anemometer. Following that procedure, the modified Jensen wake model describes more precisely the individual wake deficit at each WT as reported in [33].

90 The same assumption of the top-hat wake profile was pursued by Frandsen *et al.* [12],
91 however, the model is based on satisfying both the mass and momentum conservation equations
92 [5,12,13,15,32]. The assumption of the top-hat profile is very bold and unrealistic, as studies
93 showed that the streamwise velocity deficit profiles tends towards an axisymmetric Gaussian
94 distribution in the far-wake region [34]. As a result, Bastankhah and Porté-Agel [13] recently
95 developed an extension of the Jensen model, replacing the overly simplified top-hat profile with a
96 self-similar Gaussian profile, which presents a closer approximation for classic far-wake profile
97 [5,15,32].

98 Although Jensen [9] and Frandsen *et al.* [12] models are meant to describe the wake profile in
99 the far-wake, yet there is no explicit limitation on applying them for the whole wake, while
100 Bastankhah and Porté-Agel model [13] considered the far-wake region only, none of these
101 models accounted for the near-wake region. Therefore, the choice of either the top-hat shape
102 only or the Gaussian shape only is not quite accurate [15], as the velocity deficit increases till
103 reaching a maximum value, then decreases, due to the turbulent mixing. It was also observed that
104 the velocity profile evolves downstream of the wind turbine from a top-hat shape to a Gaussian
105 shape in the far wake [15,21,35,36]. There was no wake model providing a full demonstration of
106 the whole wake region till the recent contributions from Qian and Ishihara [14]. They proposed a
107 modified version of the Bastankhah and Porté-Agel model [13] that improves the velocity deficit
108 prediction in the near wake. In this updated model, a corrective term is added to predict realistic
109 values for near-wake wind speeds. However, this corrective term causes a violation of the mass
110 and momentum conservation [15].

111 Blondel and Cathelain [15] developed a model to overcome the violation of the conservation
112 equations by replacing the Gaussian shape with a super-Gaussian shape, which tends towards a
113 top-hat shape for high values of the super-Gaussian order n (near-wake conditions), and towards
114 the traditional Gaussian shape for $n = 2$ (far-wake conditions). As a result, it was reported that
115 the wake velocity profiles were more consistent with observations, the velocity deficit had the
116 expected form, and mass and momentum conservation equations were preserved [15]. However,
117 the model required further calibration and validation, and therefore, a newer and more accurate
118 version of the model was later proposed in Cathelain *et al.* [37], which is used in this paper, (see
119 Appendix A for the comparison between both versions).

120 The aforementioned wake models address the wake of a single WT. However, to describe the
121 wake within a wind farm where turbines operate in the wake of each other, these wake models
122 should be coupled with superposition methods to account for the interaction among multiple
123 wakes [5]. Different superposition methods have been proposed, and new ones are being
124 developed actively. Lissaman [36] method is based on the principle of linear superposition of
125 velocity deficit defined with respect to the incoming boundary layer flow speed. Afterwards,
126 Katić *et al.* [38] followed referring the velocity deficit to the incoming boundary layer flow speed
127 similar to Lissaman [36], however, with a different superposition principle that involved the linear
128 superposition of energy deficit. This superposition principle was also adopted later by Voutsinas
129 *et al.* [39], yet the velocity deficit was defined with respect to the incoming flow velocity for the
130 turbine under study. Subsequently, Niayifar and Porté-Agel [40] proposed a method with a
131 superposition principle similar to Lissaman's [36], and a velocity deficit reference similar to
132 Voutsinas *et al.* [39]. Later, Zong and Porté-Agel [41] developed an iterative method relying on
133 mass and momentum conservation considerations. Recently, Bastankhah *et al.* [42] developed a
134 new analytical model that provides an explicit wind farm solution also based on mass and
135 momentum conservation considerations.

136 The present study is considered as a continuation to the work done in Torres-Garcia *et al.* [1].
137 They processed experimental field wake measurements obtained during a 7-month ground-based
138 scanning LiDAR measurement campaign, with a set-up that enables to capture two WT wakes up
139 to $10D_r$ downstream and for a wind sector of 40° . Depending on the wind direction, WT wakes
140 experienced different interaction levels ranging from full interaction till zero interaction. This

141 long measurement campaign ensured the satisfaction of statistical convergence, which led to
142 obtaining exploitable ensemble-averaged results on wake properties. After the processing of
143 measurements, different wake characteristics were investigated such as wake centre-line position,
144 velocity deficit and the wake meandering associated with large-scale turbulent structures in the
145 incoming atmospheric flow. The associated effective operational WT conditions were not
146 considered. Supervisory Control and Data Acquisition (SCADA) data processing is therefore
147 performed following the procedures proposed in [1]. The processed SCADA data is first
148 analysed, then used as an input for the analytical wake models with the objective of checking their
149 validity and accuracy when compared to field measurements, and at the same time holding a clear
150 comparison between these models.

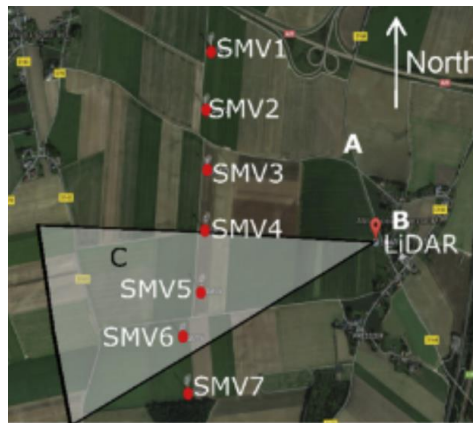
151 In the following, section 2 provides a description of the equipment and experimental set-up.
152 In section 3, the measurement processing and classification methods are described. In section 4,
153 the main results, and observations of both studies; data analysis and wake modelling, are
154 discussed. Finally, in section 5, a summary and recommendations for future research are
155 provided.

156 157 2. Experimental set-up

158 The field measurement campaign took place in the Sole du Moulin Vieux (SMV) onshore
159 wind farm, owned by Engie Green, located in Ablaincourt-Pressoir municipality in the north of
160 France in Picardy region. The wind farm consists of seven WTs, as shown in Fig. 1, sited from
161 north to south with approximate spacing of around $3.5D_r$ apart. The WTs are SENVION
162 MM82, with a diameter of $D_r = 82\text{ m}$, a hub height of $z_h = 80\text{ m}$; and a nominal power of
163 2050 kW for a nominal wind speed of $14.5\text{ m}\cdot\text{s}^{-1}$, in addition to a cut-in wind speed of
164 $3.5\text{ m}\cdot\text{s}^{-1}$. At the hub height z_h of WTs SMV6 and SMV5, a wind vane and an anemometer
165 registered the conditions at WT locations using SCADA system [1,25].

166 A pulsed scanning LiDAR (Windcube 200S) developed by Leosphere, with a speed accuracy
167 of $0.1\text{ m}\cdot\text{s}^{-1}$, was positioned 1320 m east from WT-SMV4 at ground level. The LiDAR was
168 programmed to hold scans covering azimuth angles ranging between 243° and 273°
169 (meteorological coordinates), as shown in Fig. 1.

170



171
172 **Figure 1:** The wind farm composed of seven WTs marked with red dots. A meteorological mast (A) is
173 located in the surrounding area. The location of the LiDAR is marked with B. The shadowed area, C, is
174 the top view of the area scanned by the LiDAR [1].

175 3. Methods

176 As previously mentioned, the data handling procedure of Torres-Garcia *et al.* [1] is followed
177 in this study. They considered LiDAR and the Modern-Era Retrospective analysis for Research
178 and Applications version 2 (MERRA-2) datasets. SCADA data is added to the group to have a
179 broader description of the overall situation and be able to hold comparisons. Full details about
180 the LiDAR data processing can be found in [1].

181 Before categorising the SCADA data, an hourly-averaging is performed to match the hourly
 182 MERRA-2 dataset, since SCADA data is provided as 10-minute average by default. Afterwards,
 183 the categorisation process is held according to specific environmental wind flow conditions
 184 obtained from MERRA-2. These conditions include: 1) Atmospheric stability (near-neutral), 2)
 185 Environmental wind speed ($13 \pm 1.95 \text{ m.s}^{-1}$ at 50 m height), and 3) Wind direction (four
 186 directions; 207° , 220° , 233° and $246^\circ \pm 6.4^\circ$). An additional filter based on grid availability
 187 ensures that only fully operating WT's are post-processed. Only 0.2% of the data was rejected due
 188 to this filter.

189 The ABL stability is described by Monin-Obukhov Length (L) obtained from MERRA-2.
 190 The near-neutral stability range considered for this study is $|L| \geq 300 \text{ m}$ and is based on the
 191 atmospheric stability classifications defined in Wharton *et al.* [43].

192 The wind speed (WS) used for the categorisation process is the one obtained from MERRA-2
 193 at 50 m above the ground. A reference WS $u = 13 \text{ m.s}^{-1}$ was considered. In such a
 194 configuration, stronger wake effects will occur because the WT will be working close to its
 195 nominal WS [1].

196 Four WDs were used in the study to consider different levels of interaction; starting from full
 197 interaction in case of 207° , where a wake is generated downstream of WT-SMV6 and goes all the
 198 way through WT-SMV5 whose wake includes the superimposed effects of both WT-SMV6 and
 199 WT-SMV5. As for the other three WDs, the level of interaction decreases gradually till reaching
 200 the case of zero interaction when wind flows from a direction of 246° .

202 3.1. Velocity deficit

203 There are many suggestions on how to calculate the velocity deficit (VD). Here, VD is
 204 defined as in [1]:

$$205 \quad VD_{LiDAR}(x_{WD}, z_{WD}) = \frac{u_{hub} - u_{min}(x_{WD}, z_{WD})}{u_{hub}} \quad (1)$$

206 where u_{hub} is the reference velocity at hub height extracted from the undisturbed environmental
 207 vertical velocity profile, while u_{min} is the minimum velocity at a distance (x_{WD}) downstream of
 208 the wind turbine and at an altitude z_{WD} where the LiDAR measurements were obtained. To
 209 compare the LiDAR VD evolution with the VD obtained from the engineering wake models, this
 210 formula is adapted as follows:

$$211 \quad VD_{Model}(x_{WD}, z_{WD}) = \frac{u_{SMV6} - u_{min}(x_{WD}, z_{WD})}{u_{SMV6}} \quad (2)$$

212 where u_{SMV6} is the WS measured by the anemometer on WT-SMV6.

213
 214 Another definition of VD is also employed, in the data processing part of the results. It is
 215 different to Eq. (1) because it uses the spatially resolved LiDAR classified data, thus, evolves with
 216 the downstream distance (x_{WD}). Here, VD_{SCADA} is calculated from the categorised SCADA data
 217 at the fixed locations of both WT's SMV6 and SMV5:

$$218 \quad VD_{SCADA} = \frac{u_\infty - u_w}{u_\infty} = \frac{u_{SMV6} - u_{SMV5}}{u_{SMV6}} \quad (3)$$

219
 220 where u_∞ is the undisturbed upstream velocity, while u_w is the downstream velocity in the wake
 221 of the undisturbed WT. u_∞ was taken equal to u_{SMV6} , and u_w was taken equal to u_{SMV5} , which
 222 is the WS measured by the anemometer on WT-SMV5. VD_{SCADA} depends on the position
 223 vector, $X = (x_{WD}, y_{WD}, z_{WD})$, although it is not explicitly shown in Eq. (3).
 224

225 3.2. Power deficit

226 The power deficit (PD) between the two WT's SMV5 and SMV6 is calculated similarly:

227
228
229
230
231
232
233
234
235
236
237
238
239
240
241
242
243
244
245
246
247
248
249
250
251
252
253
254
255
256
257
258
259
260
261
262
263
264
265
266
267
268
269
270
271
272

$$PD_{SCADA} = \frac{P_{SMV6} - P_{SMV5}}{P_{SMV6}} \quad (4)$$

where P_{SMV6} is the power generated by WT-SMV6, while is the power generated by WT-SMV5.

3.3. Turbulence intensity and wake added turbulence

The turbulence intensity (I_u) defines the level of velocity fluctuations due to turbulence within the flow. It is the ratio between the standard deviation of the streamwise WS (σ_u), which refers to the fluctuations around the mean value, and the mean value of streamwise WS (u) as follows for both WT's SMV6 and SMV5:

$$\begin{aligned} I_{u_{SMV6}} &= \sigma_{u_{SMV6}}/u_{SMV6} \\ I_{u_{SMV5}} &= \sigma_{u_{SMV5}}/u_{SMV5} \end{aligned} \quad (5)$$

Meanwhile, the wake added turbulence intensity is the additional turbulence induced by the WT wake, and is obtained from [5] as follows:

$$\Delta I = \sqrt{I_{wake}^2 - I_{\infty}^2} = \sqrt{I_{u_{SMV5}}^2 - I_{u_{SMV6}}^2} \quad (6)$$

where I_{wake} is the streamwise turbulence intensity in the wake measured by WT-SMV5, while $I_{u_{SMV6}}$ is the streamwise turbulence intensity measured by WT-SMV6 and considered as the free-stream turbulence intensity (I_{∞}).

3.4. Wake modelling

A mix of empirical and analytical models was used for the study. It included Aitken *et al.* [25], Jensen [9], Frandsen *et al.* [12], Bastankhah and Porté-Agel [13] because they were the ones that attracted the most attention according to [4]. That is in addition to the newly proposed model from Blondel and Cathelain [15, 37], (see Appendix A).

To analytically model wind farm flows, the aforementioned wake models are coupled with wake superposition methods to account for the wake interaction. Different techniques are available to estimate the velocity, $u(X)$, at a given position $X = (x, y, z)$ in a wind farm. The ones employed in this paper are Lissaman [36], Katić *et al.* [38], Voutsinas *et al.* [39], and Niayifar and Porté-Agel [40], (see Appendix B). The recent method from Zong and Porté-Agel [41] was not used in the current study because it is not represented in an explicit form and follows an iterative process to be incorporated, which is not computationally friendly [42]. The novel method from Bastankhah *et al.* [42] was not employed since it was mainly developed for the Gaussian model, and therefore, it would need to be adapted to the other wake models, which is not straightforward and is still under investigation.

3.5. Performance measures

A group of statistical metrics are used to measure a model performance by comparing model predictions and measurements, then quantifying the errors [44]. The ones included in the study are Fractional Bias (FB), Geometric Mean Bias (MG), Normalised Mean Squared Error (NMSE), Geometric Variance (VG), Correlation Coefficient (R), and the fraction of predictions within a factor of two of observations (FAC2), see Appendix C. A perfect model would have MG, VG, R, and FAC2 = 1; and FB and NMSE = 0. However, there is no such thing as a perfect model, because of the influence of random processes involved in the system [44,45].

4. Results

4.1. Data processing

Table 1 illustrates the ensemble-average of the WD values obtained from LiDAR measurements depicted in [1], in addition to MERRA-2, and post-processed SCADA datasets in the four WD cases. At the same time, it ensures the validity of the categorisation process held by comparing the average WD values from both SCADA and LiDAR. There is only a slight

273 difference between the SCADA values shown in this table and their corresponding LiDAR
 274 values, which confirms the validity of the process. This insignificant difference might result from
 275 the application of the grid availability condition during categorisation of the SCADA dataset.
 276 However, there is a very good agreement between the results that are within a range of about
 277 $\pm 2^\circ$, similarly as it was mentioned in [1]. The statistical convergence of SCADA data was ensured
 278 in a similar way that was reported in [1] for LiDAR data.

279 **Table 1:** Summary of characteristics of the four cases after categorisation. The cases were
 280 extracted from periods when the atmosphere was neutral according to the MERRA-2 dataset.

Case	Interaction level	Wind Direction (WD) [°]			
		LiDAR	MERRA-2	SCADA	
				SMV6	SMV5
207°	Full	208°	209°	210.3°	210.2°
220°	Partial	219°	220°	217.8°	218°
233°	Weak	233°	235°	231°	229.9°
246°	Zero	246°	245°	243.4°	241.7°

281
 282 Table 2 shows the ensemble-averaged values for different variables after categorisation.
 283 Some of these variables such as the average streamwise WS and I_u , are fed into the analytical
 284 wake models as inputs to obtain the VD in the streamwise direction within the wake. Some
 285 variables could be obtained from both MERRA-2 and SCADA datasets, while others were only
 286 obtained from either of them. There is an expected difference between the average WS values
 287 obtained from MERRA-2 and SCADA for WT-SMV6. That is because both datasets have
 288 different sources of uncertainty, and because the altitude at which the WS is given is different
 289 (50 m for MERRA-2 and 80 m for SCADA). There is a significant difference between the values
 290 obtained from WT-SMV6 and WT-SMV5, which demonstrates the wake interaction effect. Also,
 291 in the case of WS and power, there is a significant decrease between values for the two WT's
 292 when wakes fully interact ($WD = 207^\circ$), and this decrease reduces as the degree of interaction
 293 decreases. Regarding I_u , there is an increase in case of full interaction, which fades away as the
 294 interaction level decreases. The average value of L in the four WD cases shows that they lie in
 295 near-neutral ABL.
 296
 297

Table 2: Ensemble-averaged values of variables of interest after categorisation.

Case	Wind Speed (WS) [m.s ⁻¹]			Power [kW]		I_u		L [m]
	MERRA-2	SCADA		SCADA		SCADA		MERRA-2
		SMV6	SMV5	SMV6	SMV5	SMV6	SMV5	
207°	12.88	11.79	9.63	1683.55	1202.72	0.129	0.183	887.43
220°	12.74	11.80	10.12	1709.82	1343.66	0.125	0.163	1195.46
233°	12.48	11.84	11.41	1787.20	1721.89	0.107	0.114	1774.96
246°	12.61	11.45	11.16	1721.72	1723.61	0.103	0.104	1025.11

298
 299 The average streamwise WS values shown in Table 2 are used to calculate the thrust
 300 coefficient (C_T) of the WT's, which is an important parameter in the analytical wake models. C_T
 301 is computed using linear interpolation with the help of the C_T table provided in the WT
 302 manufacturer's data sheet. Table 3 shows the calculated C_T values to be fed into the wake models
 303 together with the values of WS and I_u from Table 2.
 304
 305

Table 3: Thrust coefficient (C_T) of both wind turbines in each wind direction case.

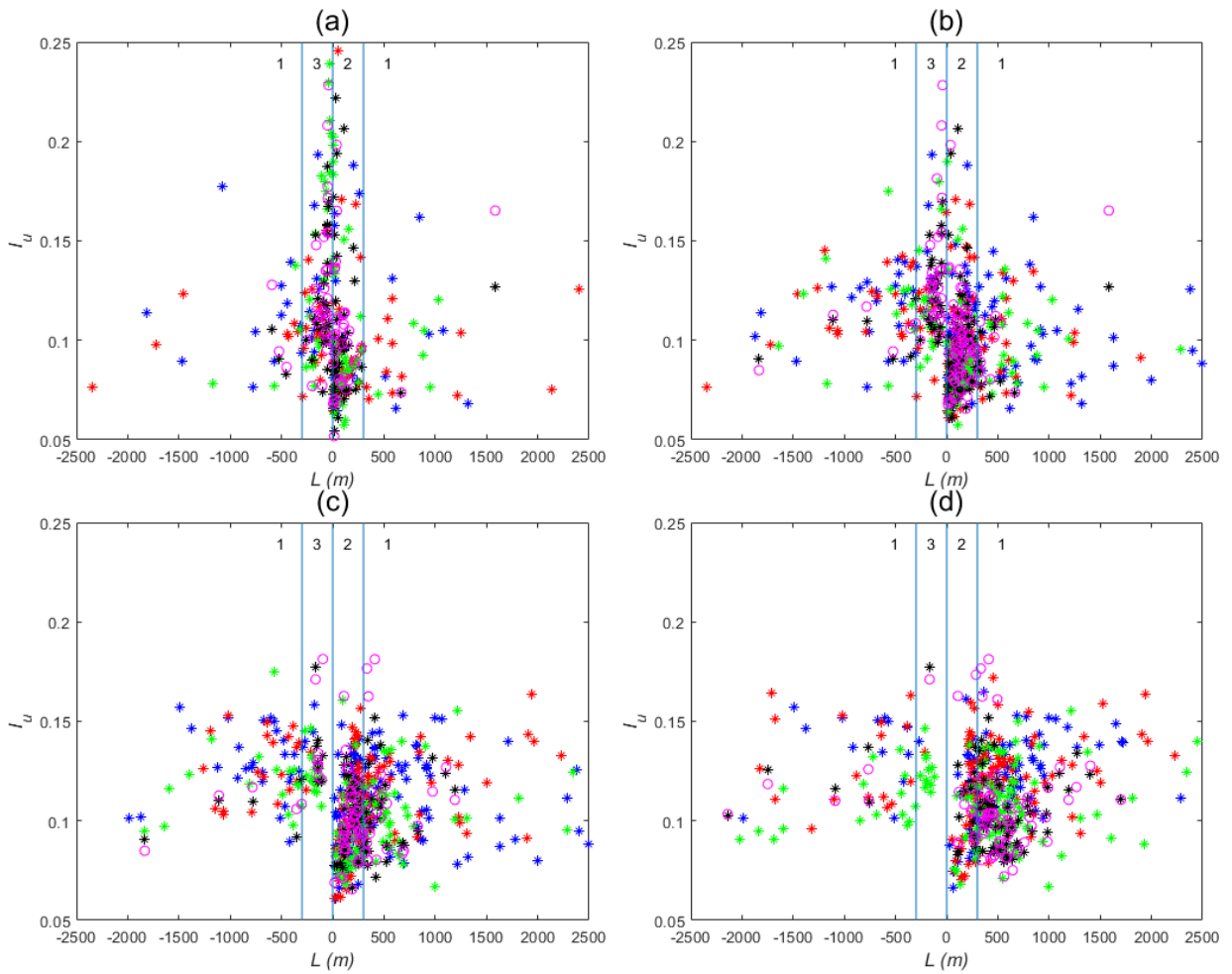
C_T	Case			
	207°	220°	233°	246°

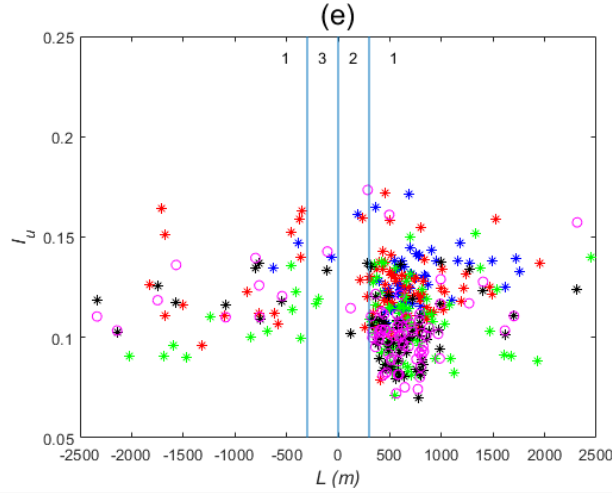
SMV6	0.5345	0.5342	0.5291	0.5765
SMV5	0.7419	0.7094	0.5811	0.6111

306
307
308
309
310
311
312
313
314
315
316
317
318

4.2. Relationship between atmospheric stability and turbulence intensity

To study the relationship between the atmospheric stability, described by L , and the free-stream turbulence intensity (I_u), three atmospheric stability cases are included with their corresponding L ranges: 1) Near-neutral ($|L| \geq 300 \text{ m}$), 2) Stable ($0 \leq L < 300 \text{ m}$), 3) Convective ($-300 \text{ m} < L < 0$). Configurations with wake interaction are neglected in this specific study, thus, the 4 WDs for WT-SMV6, and $WD = 246^\circ$ for WT-SMV5 are only considered. Five WSs are considered; $5 \text{ m} \cdot \text{s}^{-1}$, $7 \text{ m} \cdot \text{s}^{-1}$, $9 \text{ m} \cdot \text{s}^{-1}$, $11 \text{ m} \cdot \text{s}^{-1}$ and $13 \text{ m} \cdot \text{s}^{-1}$, with a tolerance of ± 1.95 . By including the different WSs, different degrees of flow advection are considered. Generally, in strong winds, atmospheric stability conditions tend to near-neutral, whereas stable and unstable winds occur more in case of lighter winds.





* WD207-SMV6 * WD220-SMV6 * WD233-SMV6 * WD246-SMV6 ○ WD246-SMV5

319 **Figure 4:** Relationship between atmospheric stability (L) and free-stream turbulence intensity
 320 (I_u) at different wind speeds for zero-wake interaction cases, where each stability range is
 321 bounded by a light blue vertical line, and the numbers 1, 2 and 3 correspond to the near-neutral,
 322 stable and convective stability ranges respectively. (a) $WS = 5 m.s^{-1}$, (b) $WS = 7 m.s^{-1}$, (c)
 323 $WS = 9 m.s^{-1}$, (d) $WS = 11 m.s^{-1}$, (e) $WS = 13 m.s^{-1}$

324 Fig. 4 illustrates the relationship between L and I_u measured by the WTs, at different WS
 325 ranges for zero-wake interaction cases. It is obvious in the figure that, as expected, the data
 326 points, migrate from near-neutral atmospheric stability at strong winds (higher WSs), towards
 327 stable and unstable stability configurations as the WS decreases. Furthermore, a trend between I_u
 328 and L , can be detected when the WS changes from $5 m.s^{-1}$ to $13 m.s^{-1}$. I_u tends towards a
 329 consistent value and presents less scatter as the atmospheric stability goes towards the neutral
 330 stability configurations. This analysis gives confidence on the strategy, which was applied in the
 331 previous [1] and the present paper, of filtering the database according to the Monin-Obukhov
 332 Length (L) deduced from MERRA-2 to extract near-neutral configurations, since the actual
 333 turbulence intensity measured onsite for the selected periods presents a homogenous and
 334 coherent level.

335
 336

337 4.3. Wake added turbulence intensity

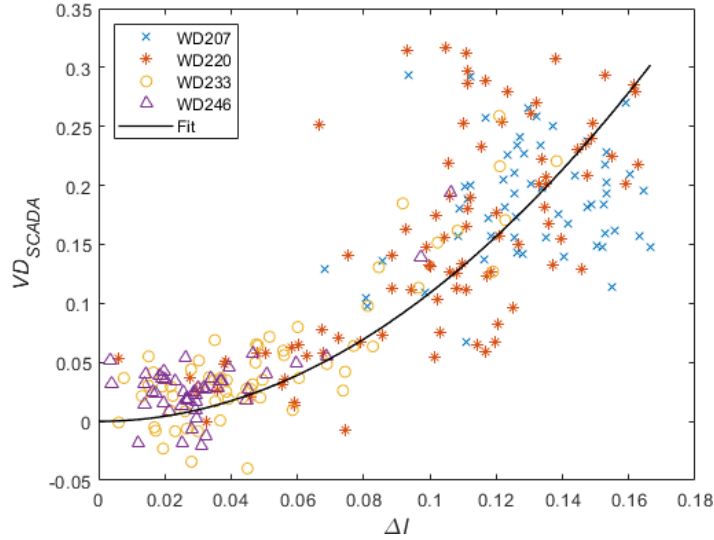
338 The effect of the wake added turbulence intensity (ΔI) on the velocity deficit (VD) and
 339 the power deficit (PD) was investigated. The VD and PD are obtained from the categorised
 340 SCADA data in near-neutral atmospheric stability conditions.

341

342 4.3.1. Wake added turbulence intensity and velocity deficit

343 The relationship between the VD, obtained from Eq. (3), and ΔI , calculated using Eq. (6),
 344 was investigated (Fig. 5). Fig. 5 comprises all the four cases of the wake interaction presented in
 345 this study to have a global view of the evolution between the two variables. The distribution of
 346 VD with respect to ΔI is in line with the fact that for the case of full-wake interaction (WD207°),
 347 ΔI is the largest, which reflects on the data scatter also, as the degree of scatter is high. Then it
 348 decreases gradually with the reduction in the degree of wake interaction. As there is less ΔI and
 349 scatter in case of the partial-wake interaction (WD220°) than the full interaction case. This is
 350 followed by the weak interaction case (WD233°), and finally, the zero interaction case (WD246°)
 351 with the lowest ΔI and data scatter.

352



353
 354 **Figure 5:** Curve fitting of the evolution of VD_{SCADA} with ΔI at different wake interaction degrees
 355 in near-neutral stability conditions
 356

357 It is noticed that there is a trend between both variables. So, curve fitting was performed to
 358 check the best fit for the data as shown in Fig. 5. It was found that the data follows an
 359 exponential trend:

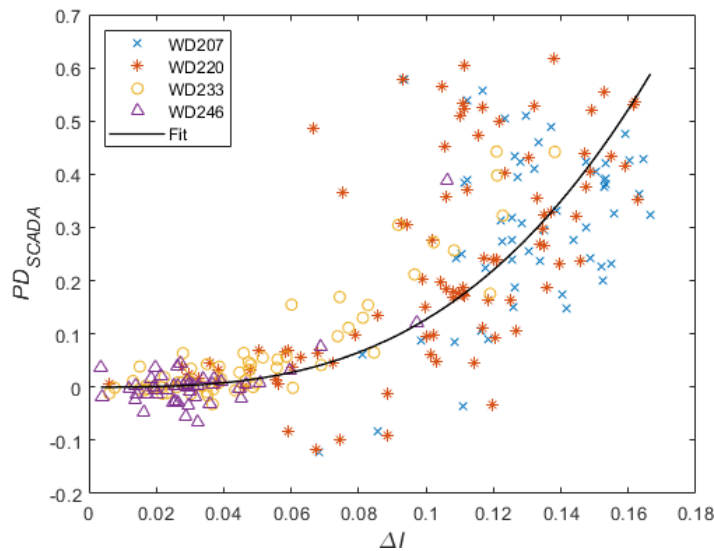
$$VD_{SCADA} = a(e^{b\Delta I^2} - 1) \quad (5)$$

360 where a and b are two fitted coefficients (with 95% confidence bounds); with $a = 526.2$ and
 361 $b = 0.0207$. Furthermore, the statistical measures of the goodness of fit are $SSE = 0.8336$, $R -$
 362 $square = 0.6081$, $Adjusted R - square = 0.6066$, and $RMSE = 0.05695$. More details about
 363 those statistical measures can be found in [46].
 364

365 The fit assessment metrics are not the best, especially, the confidence bounds and SSE
 366 because of the data scatter.
 367

368 4.3.2. Wake added turbulence intensity and power deficit

369 The relationship between the PD, obtained from Eq. (4), and ΔI , calculated using Eq. (6),
 370 was investigated (Fig. 6).
 371



372
 373 **Figure 6:** Curve fitting of the evolution of PD_{SCADA} with ΔI at different wake interaction degrees
 374 in near-neutral stability conditions
 375

376 The trend in Fig. 6 looks similar to the one in Fig. 5, which is expected since the
 377 generated power is a function of the cube of the WS. Consequently, the same process was held
 378 for PD, and a curve fitting was performed. It was found that the data follows an exponential
 379 trend like in VD case:

$$380 \quad PD_{SCADA} = c(e^{d\Delta I^3} - 1) \quad (6)$$

381 where c and d are two fitted coefficients (with 95% confidence bounds); with $c = 999.4$
 382 and $d = 0.1275$. Moreover, the statistical measures of the goodness of fit are $SSE = 5.147$, $R -$
 383 $square = 0.4885$, $Adjusted R - square = 0.4865$, and $RMSE = 0.1415$.

384 Like in the case of VD, the fit assessment metrics are not good, which is expected with
 385 such scatter.

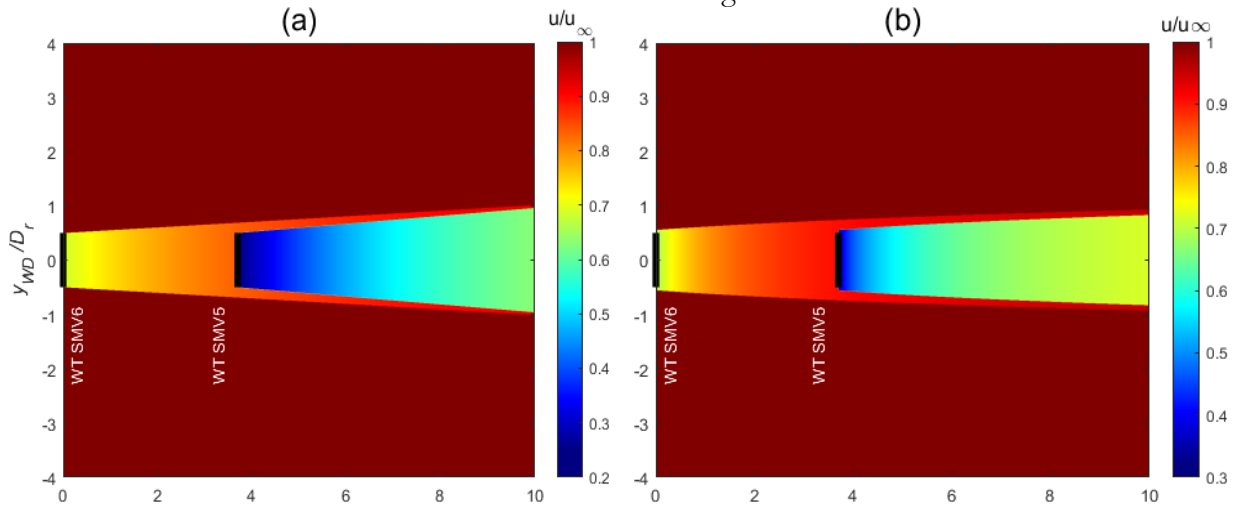
386 Both laws in Eq. (5) and Eq. (6) are not universal since they will change with other
 387 parameters that have not been considered here. Mainly, the relative position of wind turbines,
 388 their operating point, and the atmospheric stability conditions. However, it is shown that a clear
 389 trend can be extracted, giving confidence in the present handling of categorised SCADA data.
 390 Additionally, this feature could be used to better predict the added turbulence within the wakes,
 391 or to calibrate the added turbulence intensity models used in combination with wake
 392 superposition models. These aspects are out of the scope of the present paper but require further
 393 investigation in this direction.

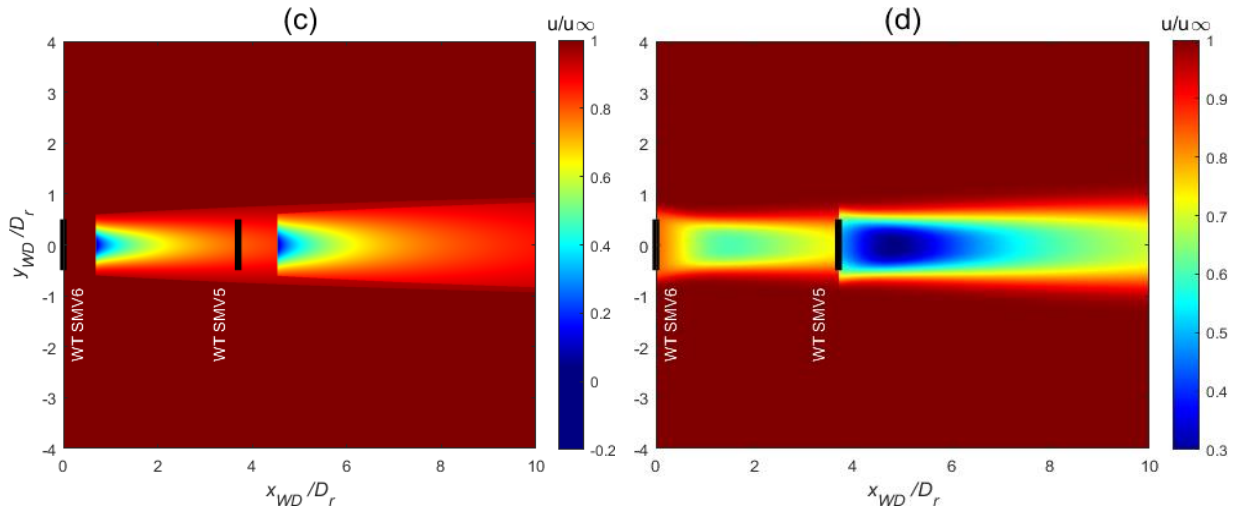
394 395 4.4. Comparison of wake models

396 In this part, a distinct study of the wakes, applying the categorisation process in section 3,
 397 is held where a comparison between the different engineering wake models is conducted.

398 399 4.4.1. Wake contours

400 Some wake contours are shown for visualisation purposes to replicate what was done in
 401 [1] but using the analytical wake models. For this matter, the normalised velocity contours for the
 402 different wake models are shown in the following figures, showing the wake evolution in the
 403 horizontal streamwise and crosswise directions at hub height.

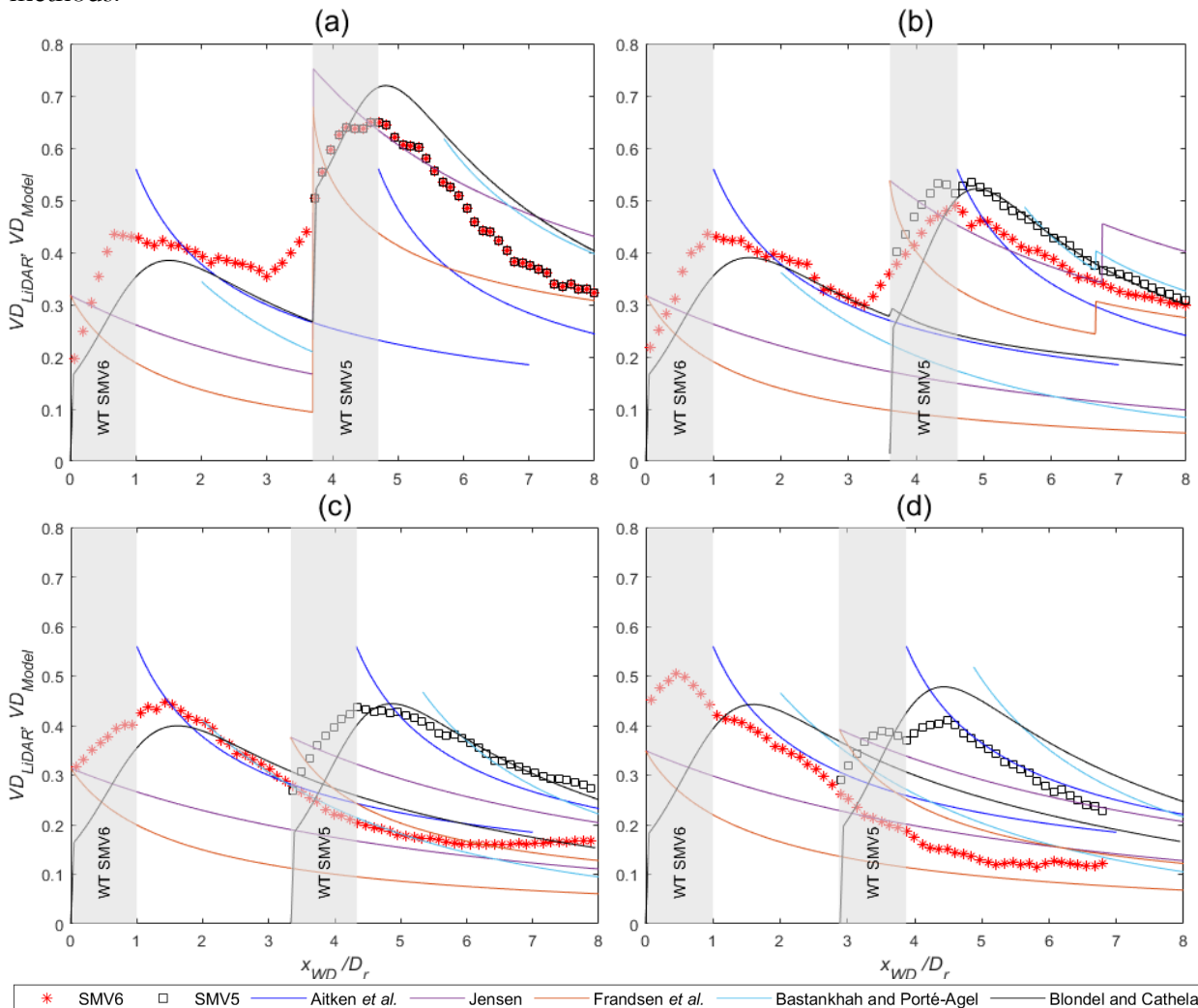




404 **Figure 7:** Normalised velocity contours at $WD = 207^\circ$ produced using different wake models,
 405 (a) Jensen, (b) Frandsen *et al.*, (c) Bastankhah and Porté-Agel, (d) Blondel and Cathelain.

406 **4.4.2. Velocity deficit from analytical wake models and field measurements**

407 In this part, the VDs obtained from the analytical wake models are compared with the one
 408 obtained from the field measurements (LiDAR). This was realised by extracting the velocity at
 409 the wake centre assumed at $y = 0$ from the wake contours in Section 4.4.1. The objective is to
 410 have a global overview on the performance of the different wake models and superposition
 411 methods.



412 **Figure 8:** Velocity deficit profiles along the wake center ($y = 0$) for different wake models and field measurements (LiDAR). The legend indicates the models used: SMV6 (red asterisk), SMV5 (open square), Aitken *et al.* (blue line), Jensen (purple line), Frandsen *et al.* (orange line), Bastankhah and Porté-Agel (cyan line), and Blondel and Cathelain (black line).

413 **Figure 8:** Comparison between the evolution of the normalised velocity deficits (VD) calculated
414 at $y = 0$ and the measurement altitude (z), and obtained from the different engineering wake
415 models superimposed by Lissaman method (VD_{Model}) with the one obtained experimentally
416 (VD_{LiDAR}) in the four WDs depicted from Torres-Garcia *et al.* [1], with respect to the
417 normalised downstream distance (x/D_r). (a) $WD = 207^\circ$, (b) $WD = 220^\circ$, (c) $WD = 233^\circ$, (d)
418 $WD = 246^\circ$.

419 Fig. 8 shows the comparison between the VD obtained from the different analytical wake
420 models, with respect to the VD presenting the field (LiDAR) measurements, calculated using Eq.
421 (1) for different x/D_r in each of the four WD configurations. The variation in the altitude of
422 each LiDAR data point, (see Appendix D), was considered when applying the wake models to
423 have a reliable comparison [1]. The grey rectangles in the figure mark the area of influence of the
424 WT's where the LiDAR measurements were contaminated by reflection on the rotor [1]. The
425 VD s obtained from the analytical wake models were calculated at the wake centre assumed at
426 $y = 0$ in the horizontal crosswise direction, which is the location of maximal velocity deficit. The
427 VD s extracted from the scanning LiDAR measurements also represent the maximum VD within
428 the wake, but its y -coordinate can be slightly different than 0 [1]. However, it is considered that
429 this does not play an important role in the comparison.

430 The sudden increase in VD noticed at WT-SMV5 location in Fig. 8a and 8b corresponds to
431 wake interaction with full-wake overlapping for $WD = 207^\circ$ and partial one for $WD = 220^\circ$.
432 Even though there is a small interaction in case of $WD = 233^\circ$ shown in Fig. 8c, there is no
433 obvious increase in the VD like the ones occurring in the overlapping cases, yet there is an
434 interaction which can be detected far downstream as the wake evolves for further distance.

435 Jensen model neither accounts for the induction zone, nor the near-wake zone. This is not
436 realistic as its VD is always decreasing downstream for a single WT case. In case of a single wake
437 (WT-SMV6), there is always an underestimation of the VD because of the top-hat distribution
438 assumption for wake VD profiles. As it seems to depend on the wake interaction level between
439 WT-SMV6 and WT-SMV5, ranging between 10% - 20% for full interaction ($WD = 207^\circ$).
440 However, this range decreases as the wake interaction level decreases. This is because it is
441 affected by the weakening of the induction zone of WT-SMV5. In case of the wake downstream
442 of WT-SMV5, it depends on the wake interaction level. If there is wake interaction, there is an
443 overestimation, otherwise the underestimation continues like in case of WT-SMV6.

444 Frandsen model does not consider the induction and near-wake zones like Jensen model, yet
445 nothing was mentioned in the literature about the correct starting downstream position of its
446 application. It also underestimates VD for single wake (WT-SMV6), also because of the top-hat
447 assumption like in case of Jensen, but in this case, the degree of underestimation is even greater
448 than that of Jensen's. Even for the wake of WT-SMV5, underestimation continues, but in this
449 case the wake interaction has the opposite effect on the degree of underestimation, as it is the
450 smallest in case of full interaction, then increases as the interaction level decreases.

451 Bastankhah and Porté-Agel model is developed to be applicable only in the far-wake. That is
452 why its starting point of application is at a downstream distance of $2D_r$ from the WT according
453 to [13]. Overall, this model seems to perform well, and better than Jensen and Frandsen models.
454 Its overall performance is good either for a single wake (WT-SMV6), or for the superimposed
455 wake (WT-SMV5). It seems that for a single wake, it underestimates the VD with a smaller
456 percentage than that from Jensen and Frandsen *et al.* models, then this percentage decreases as
457 wake interaction decreases. The underestimation continues decreasing as long as there is an
458 interaction of wakes. Once the wake interaction disappears, the model overestimates the VD . On
459 the other hand, for the superimposed wake of WT-SMV5, there is always an overestimation of
460 VD . In some cases of interaction like partial and weak interaction cases, the model performs very
461 well compared to the full and zero interaction cases.

462 Blondel and Cathelain model accounts for the near-wake in addition to the far-wake zone as
 463 shown in Fig. 8. Generally, it performs in a similar manner as Bastankhah and Porté-Agel but
 464 produces closer values to the LiDAR measurements. It underestimates the VD for single wake
 465 (WT-SMV6) looking at the full-wake interaction, but the underestimation decreases as the wake
 466 interaction decreases, then overestimation occurs when interaction vanishes. For the
 467 superimposed wake, the model does very well in case of partial and weak interaction compared to
 468 the full and zero interaction cases where there is an overestimation. Overall, the model performs
 469 significantly well in the cases of partial and weak-wake interaction compared to the other two
 470 cases.

471 Additionally, Aitken *et al.* model performs very well generally in the single wake cases (WT-
 472 SMV6), and in the superimposed wake (WT-SMV5) in some configurations.

474 4.4.3. Performance assessment of analytical wake models

475 The performances of the analytical wake models and the wake superposition methods are
 476 investigated by applying the performance metrics to find out which model returns the closest
 477 results to the field measurements.

478 Since the purpose of the analytical wake models is to describe the wake of a single wind
 479 turbine, the performance metrics for the zero-wake interaction case were firstly computed, to
 480 specify which wake model works the best when compared to the field measurements. The case of
 481 zero-wake interaction comprises WT-SMV6 in the four WD configurations, in addition to WT-
 482 SMV5 for the $WD = 246^\circ$ configuration as shown in Table 4. Afterwards, the metrics for the
 483 cases with wake interaction were calculated to specify the wake superposition method that works
 484 best with the specified wake model as shown in Table 5.

485 During calculating the performance metrics for the different wake models for WT-SMV6, the
 486 points lying in the induction zone upstream of WT-SMV5 (which starts with the sudden increase
 487 in VD of the single wake (WT-SMV6)) were disregarded. So, they should not be considered while
 488 checking the figures. However, for superimposed wake (WT-SMV5), the performance of the
 489 different superposition methods becomes important.

491 **Table 4:** Performance metrics for the best wake model specification. The model with the
 492 optimum values is shown together with its absolute values of the maximum and minimum
 493 deviations from the ideal value of each metric.

Case	SMV6 (4WDs) & SMV5 (WD246°)
Interaction level	Zero interaction
FB ($-2 < FB < 2$)	Blondel and Cathelain (0.03 - 0.23)
MG ($0.75 < MG < 1.25$)	Blondel and Cathelain (0.79 - 1.11)
NMSE ($NMSE \leq 0.5$)	Blondel and Cathelain (0.005 - 0.05)
VG ($0.75 < VG < 1.25$)	Blondel and Cathelain (1.004 - 1.06)
R (Ideal = 1)	Jensen (0.9 - 0.93)
Mean FAC2 (Ideal =1)	Blondel and Cathelain (0.9 - 1.3)

494 Table 4 summarises the performance metrics calculated for all the wake models used in the
 495 study. For each metric, the wake model with the best results was chosen. According to Table 4,
 496 Blondel and Cathelain model dominates significantly in almost all the metrics. It returns the
 497 closest result to the ideal value of each metric. Therefore, Blondel and Cathelain model is
 498 considered as the best performing wake model. Consequently, the wake superposition method
 499 which works best with Blondel and Cathelain model is specified afterwards in Table 5.

502 **Table 5:** Performance measures for the best wake superposition method specification with
 503 Blondel and Cathelain wake model. The method with the optimum value in each case is shown
 504 together with the value of the metric.

Case	SMV5 (WD207°)	SMV5 (WD220°)	SMV5 (WD233°)
Interaction level	Full interaction	Partial interaction	Weak interaction
FB (-2 < FB < 2)	Katić <i>et al.</i> (0.14)	Lissaman (0.01)	Lissaman (0.001)
MG (0.75 < MG < 1.25)	Lissaman (0.82)	Lissaman (1.02)	Lissaman (1.003)
NMSE (NMSE ≤ 0.5)	Lissaman (0.03)	Lissaman (0.001)	Lissaman (0.002)
VG (0.75 < VG < 1.25)	Lissaman (1.042)	Lissaman (1.002)	Lissaman (1.002)
R (Ideal = 1)	Lissaman (0.96)	Lissaman (0.96)	Katić <i>et al.</i> (0.96)
Mean FAC2 (Ideal = 1)	Katić <i>et al.</i> (0.91)	Lissaman (0.982)	Lissaman (0.997)

Therefore, according to Tables 4 and 5, Blondel and Cathelain model coupled with Lissaman wake superposition method was concluded to perform the best. The same procedure used to generate Table 5, was used for Jensen, Frandsen *et al.* and Bastankhah and Porté-Agel models to have the comparison figures with each wake model coupled with the wake superposition method that works best with it. It was found that Lissaman method works best with Jensen, Frandsen *et al.* and Bastankhah and Porté-Agel models too.

5. Conclusions and future work

A scanning LiDAR measurement campaign was conducted for a 7-month duration in SMARTEOLE project to study the wake behaviour and characteristics. The campaign was set up such that the wakes of two WT's were measured. Four WDs were selected (207°, 220°, 233° and 246°) corresponding to different wake interaction levels. Only near-neutral atmospheric boundary layer was considered in the wake models comparison study.

MERRA-2 dataset was used for the categorisation of data, and the post-processing of the scanning LiDAR measurements was previously done by Torres-Garcia *et al.* [1].

The aim of the present study was to validate the engineering wake models in comparison with full scale WT's wake evolution obtained with scanning LiDAR measurements. This required complementing the LiDAR measurements with WT's SCADA data. The main objective was to obtain the operational and environmental data acquired by SCADA during the LiDAR measurement campaign to feed the analytical wake models to mitigate the uncertainties on specific inputs as the turbulence intensity and the WT thrust coefficient. However, another secondary objective was to find or validate relationships between the specific data such as the atmospheric stability and the free-stream turbulence intensity, and velocity and power deficits with respect to the wake added turbulence intensity.

The correlation between the atmospheric thermal stability and the free-stream turbulence intensity (I_u) was investigated. Different WSs were involved to consider different wind strengths, and, thus, different atmospheric stability conditions: neutral, stable, and convective atmospheric boundary layers, expressed with Monin-Obukhov Length (L). As expected, a smaller scatter was noticed in I_u in case of high winds, and the atmospheric stability conditions tended towards the neutral stability configuration. However, in case of light winds, there was much more scatter in I_u , and the atmospheric stability conditions tended towards convective or stable configurations.

While investigating the relationship between the wake added turbulence intensity (ΔI), a clear trend was detected between the velocity and power deficits with respect to ΔI . Consequently, empirical equations relating those variables were obtained by curve fitting of the data. It was found that both velocity and power deficits follow an exponential trend with respect to ΔI .

Before applying the engineering wake models coupled with the wake superposition methods, a performance assessment of the different wake models was held first by calculating different statistical error metrics in case of zero-wake interaction, which showed how close the wake models predictions compared to the field LiDAR measurements. Blondel and Cathelain wake model was the one with the best results compared to the rest of the models. Afterwards, another performance assessment of the wake superposition methods in case of wake interaction, when coupled with Blondel and Cathelain model, was conducted. Based on the assessment results,

548 Lissaman superposition method was found to perform the best with Blondel and Cathelain
549 model.

550 Regarding future work, the usage of the more sophisticated ERA5 reanalysis would be better
551 suited, as it has proven its superiority [47]. Indeed, the ERA5 reanalysis is based on a refined grid
552 with higher spatial and temporal resolutions. Furthermore, the data is at **100 m**, which is closer
553 to the hub height than the data from MERRA-2 at **50 m**. Also, it is important to study other
554 atmospheric stability conditions as in Aubrun *et al.* [28] since atmospheric stability is not properly
555 considered neither in experiments nor in analytical wake models [5].
556

557 558 **Acknowledgments**

559 The data presented here was obtained within the SMARTEOLE project (ANR-14-CE05-0034)
560

561 **References**

- 562 [1] Torres-Garcia, E., Aubrun, S., Coupiac, O., Girard, N. and Boquet, M., 2019. Statistical
563 characteristics of interacting wind turbine wakes from a 7-month LiDAR measurement
564 campaign. *Renewable energy*, 130, pp.1-11. <https://doi.org/10.1016/j.renene.2018.06.030>
- 565 [2] Barthelmie, R.J., Frandsen, S.T., Nielsen, M.N., Pryor, S.C., Rethore, P.E. and Jørgensen,
566 H.E., 2007. Modelling and measurements of power losses and turbulence intensity in wind
567 turbine wakes at Middelgrunden offshore wind farm. *Wind Energy: An International Journal
568 for Progress and Applications in Wind Power Conversion Technology*, 10(6), pp.517-528.
569 <https://doi.org/10.1002/we.238>
- 570 [3] Barthelmie, R.J. and Jensen, L.E., 2010. Evaluation of wind farm efficiency and wind turbine
571 wakes at the Nysted offshore wind farm. *Wind Energy*, 13(6), pp.573-586.
572 <https://doi.org/10.1002/we.408>
- 573 [4] El- Asha, S., Zhan, L. and Iungo, G.V., 2017. Quantification of power losses due to wind
574 turbine wake interactions through SCADA, meteorological and wind LiDAR data. *Wind
575 Energy*, 20(11), pp.1823-1839. <https://doi.org/10.1002/we.2123>
- 576 [5] Porté-Agel, F., Bastankhah, M. and Shamsoddin, S., 2020. Wind-turbine and wind-farm
577 flows: a review. *Boundary-Layer Meteorology*, 174(1), pp.1-59.
578 <https://doi.org/10.1007/s10546-019-00473-0>
- 579 [6] Burton, T., Sharpe, D., Jenkins, N. and Bossanyi, E., 2001. *Wind energy handbook* (Vol. 2).
580 New York: Wiley.
- 581 [7] Medici, D., Ivanell, S., Dahlberg, J.Å. and Alfredsson, P.H., 2011. The upstream flow of a
582 wind turbine: blockage effect. *Wind Energy*, 14(5), pp.691-
583 697. <https://doi.org/10.1002/we.451>
- 584 [8] Simley, E., Angelou, N., Mikkelsen, T., Sjöholm, M., Mann, J. and Pao, L.Y., 2016.
585 Characterization of wind velocities in the upstream induction zone of a wind turbine using
586 scanning continuous-wave lidars. *Journal of Renewable and Sustainable Energy*, 8(1),
587 p.013301. <https://doi.org/10.1063/1.4940025>
- 588 [9] Jensen, N.O., 1983. A note on wind turbine interaction Technical report Risø-M-2411.
589 Roskilde (Denmark): Risø National Laboratory.
- 590 [10] Ainslie, J.F., 1988. Calculating the flowfield in the wake of wind turbines. *Journal of Wind
591 Engineering and Industrial Aerodynamics*, 27(1-3), pp.213-224.
- 592 [11] Larsen, G.C., 1988. A simple wake calculation procedure. Risø National Laboratory.
- 593 [12] Frandsen, S., Barthelmie, R., Pryor, S., Rathmann, O., Larsen, S., Højstrup, J. and
594 Thøgersen, M., 2006. Analytical modelling of wind speed deficit in large offshore wind
595 farms. *Wind Energy: An International Journal for Progress and Applications in Wind Power
596 Conversion Technology*, 9(1- 2), pp.39-53. <https://doi.org/10.1002/we.189>
- 597 [13] Bastankhah, M. and Porté-Agel, F., 2014. A new analytical model for wind-turbine wakes.
598 *Renewable Energy*, 70, pp.116-123. <https://doi.org/10.1016/j.renene.2014.01.002>

- 599 [14] Qian, G.W. and Ishihara, T., 2018. A new analytical wake model for yawed wind turbines.
600 Energies, 11(3), p.665. <https://doi.org/10.3390/en11030665>
- 601 [15] Blondel, F. and Cathelain, M., 2020. An alternative form of the super-Gaussian wind turbine
602 wake model. *Wind Energy Science*, 5(3), pp.1225-1236. [https://doi.org/10.5194/wes-5-1225-](https://doi.org/10.5194/wes-5-1225-2020)
603 [2020](https://doi.org/10.5194/wes-5-1225-2020)
- 604 [16] Wu, Y.T. and Porté-Agel, F., 2011. Large-eddy simulation of wind-turbine wakes: evaluation
605 of turbine parametrisations. *Boundary-layer meteorology*, 138(3), pp.345-366.
606 <https://doi.org/10.1007/s10546-010-9569-x>
- 607 [17] Wu, Y.T. and Porté-Agel, F., 2012. Atmospheric turbulence effects on wind-turbine wakes:
608 An LES study. *energies*, 5(12), pp.5340-5362. <https://doi.org/10.3390/en5125340>
- 609 [18] Wu, Y.T. and Porté-Agel, F., 2013. Simulation of turbulent flow inside and above wind
610 farms: model validation and layout effects. *Boundary-layer meteorology*, 146(2), pp.181-205.
611 <https://doi.org/10.1007/s10546-012-9757-y>
- 612 [19] Wu, Y.T. and Porté-Agel, F., 2015. Modeling turbine wakes and power losses within a wind
613 farm using LES: An application to the Horns Rev offshore wind farm. *Renewable Energy*,
614 75, pp.945-955. <https://doi.org/10.1016/j.renene.2014.06.019>
- 615 [20] Stevens, R.J., Martínez-Tossas, L.A. and Meneveau, C., 2018. Comparison of wind farm large
616 eddy simulations using actuator disk and actuator line models with wind tunnel experiments.
617 *Renewable energy*, 116, pp.470-478. <https://doi.org/10.1016/j.renene.2017.08.072>
- 618 [21] Aubrun, S., Loyer, S., Hancock, P.E. and Hayden, P., 2013. Wind turbine wake properties:
619 Comparison between a non-rotating simplified wind turbine model and a rotating model.
620 *Journal of Wind Engineering and Industrial Aerodynamics*, 120, pp.1-8.
621 <https://doi.org/10.1016/j.jweia.2013.06.007>
- 622 [22] Bastankhah, M. and Porté-Agel, F., 2017. Wind tunnel study of the wind turbine interaction
623 with a boundary-layer flow: Upwind region, turbine performance, and wake region. *Physics*
624 *of Fluids*, 29(6), p.065105. <https://doi.org/10.1063/1.4984078>
- 625 [23] Hyvärinen, A., Lacagnina, G. and Segalini, A., 2018. A wind- tunnel study of the wake
626 development behind wind turbines over sinusoidal hills. *Wind Energy*, 21(8), pp.605-617.
627 <https://doi.org/10.1002/we.2181>
- 628 [24] Iungo, G.V., Wu, Y.T. and Porté-Agel, F., 2013. Field measurements of wind turbine wakes
629 with lidars. *Journal of Atmospheric and Oceanic Technology*, 30(2), pp.274-287.
630 <https://doi.org/10.1175/JTECH-D-12-00051.1>
- 631 [25] Aitken, M.L., Banta, R.M., Pichugina, Y.L. and Lundquist, J.K., 2014. Quantifying wind
632 turbine wake characteristics from scanning remote sensor data. *Journal of Atmospheric and*
633 *Oceanic Technology*, 31(4), pp.765-787. <https://doi.org/10.1175/JTECH-D-13-00104.1>
- 634 [26] Aitken, M.L. and Lundquist, J.K., 2014. Utility-scale wind turbine wake characterization
635 using nacelle-based long-range scanning lidar. *Journal of Atmospheric and Oceanic*
636 *Technology*, 31(7), pp.1529-1539. <https://doi.org/10.1175/JTECH-D-13-00218.1>
- 637 [27] Kumer, V.M., Reuder, J., Svardal, B., Sætre, C. and Eecen, P., 2015. Characterisation of
638 single wind turbine wakes with static and scanning WINTWEX-W LiDAR data. *Energy*
639 *Procedia*, 80, pp.245-254. <https://doi.org/10.1016/j.egypro.2015.11.428>
- 640 [28] Aubrun, S., Torres-Garcia, E., Boquet, M., Coupiac, O. and Girard, N., 2018. In Statistical
641 Analysis of a Field Database to Study Stability Effects on Wind Turbine Wake Properties. In
642 *Journal of Physics: Conference Series* (Vol. 1037, No. 7, p. 072047).
643 <https://doi.org/10.1088/1742-6596/1037/7/072047>
- 644 [29] Zhang, W., Markfort, C.D. and Porté-Agel, F., 2013. Wind-turbine wakes in a convective
645 boundary layer: A wind-tunnel study. *Boundary-layer meteorology*, 146(2), pp.161-179.
646 <https://doi.org/10.1007/s10546-012-9751-4>
- 647 [30] Iungo, G.V. and Porté-Agel, F., 2014. Volumetric lidar scanning of wind turbine wakes
648 under convective and neutral atmospheric stability regimes. *Journal of Atmospheric and*
649 *Oceanic Technology*, 31(10), pp.2035-2048. <https://doi.org/10.1175/JTECH-D-13-00252.1>

- 650 [31] Aitken, M.L., Kosović, B., Mirocha, J.D. and Lundquist, J.K., 2014. Large eddy simulation of
651 wind turbine wake dynamics in the stable boundary layer using the Weather Research and
652 Forecasting Model. *Journal of Renewable and Sustainable Energy*, 6(3), p.033137.
653 <https://doi.org/10.1063/1.4885111>
- 654 [32] Stevens, R.J. and Meneveau, C., 2017. Flow structure and turbulence in wind farms. *Annual
655 review of fluid mechanics*, 49. <https://doi.org/10.1146/annurev-fluid-010816-060206>
- 656 [33] Duc, T., Coupiac, O., Girard, N., Giebel, G., and Göçmen, T.: Local turbulence
657 parameterization improves the Jensen wake model and its implementation for power
658 optimization of an operating wind farm, *Wind Energ. Sci.*, 4, 287–302.
659 <https://doi.org/10.5194/wes-4-287-2019,2019>
- 660 [34] Medici, D. and Alfredsson, P.H., 2006. Measurements on a wind turbine wake: 3D effects
661 and bluff body vortex shedding. *Wind Energy: An International Journal for Progress and
662 Applications in Wind Power Conversion Technology*, 9(3), pp.219-
663 236. <https://doi.org/10.1002/we.156>
- 664 [35] Sørensen, J.N., Mikkelsen, R.F., Henningson, D.S., Ivanell, S., Sarmast, S. and Andersen, S.J.,
665 2015. Simulation of wind turbine wakes using the actuator line technique. *Philosophical
666 Transactions of the Royal Society A: Mathematical, Physical and Engineering Sciences*,
667 373(2035), p.20140071. <https://doi.org/10.1098/rsta.2014.0071>
- 668 [36] Lissaman, P.B.S., 1979. Energy effectiveness of arbitrary arrays of wind turbines. *Journal of
669 Energy*, 3(6), pp.323-328. <https://doi.org/10.2514/3.62441>
- 670 [37] Cathelain, M., Blondel, F., Joulin, P.A. and Bozonnet, P., 2020, September. Calibration of a
671 super-Gaussian wake model with a focus on near-wake characteristics. In *Journal of Physics:
672 Conference Series* (Vol. 1618, No. 6, p. 062008). IOP Publishing.
673 <https://doi.org/10.1088/1742-6596/1618/6/062008>
- 674 [38] Katic, I., Højstrup, J. and Jensen, N.O., 1986, October. A simple model for cluster
675 efficiency. In *European wind energy association conference and exhibition* (Vol. 1, pp. 407-
676 410).
- 677 [39] Voutsinas, S., Rados, K. and Zervos, A., 1990. On the analysis of wake effects in wind parks.
678 *Wind Engineering*, pp.204-219. Available at: <https://www.jstor.org/stable/43749429>
679 (Accessed 25 November 2020)
- 680 [40] Niayifar, A. and Porté-Agel, F., 2016. Analytical modeling of wind farms: A new approach
681 for power prediction. *Energies*, 9(9), p.741. <https://doi.org/10.3390/en9090741>
- 682 [41] Zong, H. and Porté-Agel, F., 2020. A momentum-conserving wake superposition method
683 for wind farm power prediction. *Journal of Fluid Mechanics*, 889.
684 <https://doi.org/10.1017/jfm.2020.77>
- 685 [42] Bastankhah, M., Welch, B.L., Martínez-Tossas, L.A., King, J. and Fleming, P., 2021.
686 Analytical solution for the cumulative wake of wind turbines in wind farms. *Journal of Fluid
687 Mechanics*, 911. <https://doi.org/10.1017/jfm.2020.1037>
- 688 [43] Wharton, S. and Lundquist, J.K., 2010. Atmospheric stability impacts on power curves of
689 Tall wind turbines-an Analysis of a West Coast North American wind farm (No. LLNL-TR-
690 424425). Lawrence Livermore National Lab. (LLNL), Livermore, CA (United States).
691 <https://doi.org/10.2172/973337>
- 692 [44] Patryla, L. and Galeriu, D., 2011. Statistical performances measures—models comparison.
693 CEA: Paris, France.
- 694 [45] Chang, J.C. and Hanna, S.R., 2004. Air quality model performance evaluation. *Meteorology
695 and Atmospheric Physics*, 87(1-3), pp.167-196. <https://doi.org/10.1007/s00703-003-0070-7>
- 696 [46] Toolbox, C.F., 2001. For Use with MATLAB; [user's Guide]. Natick, MA: MathWorks.
- 697 [47] Jourdir, B., 2020. Evaluation of ERA5, MERRA-2, COSMO-REA6, NEWA and AROME
698 to simulate wind power production over France. *Advances in Science and Research*, 17,
699 pp.63-77. <https://doi.org/10.5194/asr-17-63-2020>
- 700

701 - **Appendix A: Engineering wake models**

702 • **Aitken *et al.* model:**

703 An empirical wake model that assumes a power-law relationship of the VD with
 704 downstream distance x_{WD} . The model was developed based on the fitting of a
 705 collection of measurements dated between 1981 and 2013 [1,25], and defined as:
 706

707
$$VD(x_{WD}) = 0.56 \left(\frac{x_{WD}}{D_r} \right)^{-0.57} \quad (A.1)$$

708 • **Jensen model:**

709 Jensen model is derived by applying the conservation of mass to a control volume
 710 downwind of the wind turbine, and then using Betz theory to relate the wind speed
 711 just behind the rotor to the turbine thrust coefficient C_T [5,38]. It neglects the near-
 712 wake region, and assumes a top-hat distribution, for the velocity deficit in the wake
 713 for the sake of simplicity [5,9]. The normalized velocity deficit based on this model is
 714 given by:

715
$$\frac{\Delta u}{u_o} = \frac{1 - \sqrt{1 - C_T}}{(1 + 2k\tilde{x})^2} \quad (A.1)$$

716 where u_o is the mean incoming wind speed, and obtained from SCADA for WT-
 717 SMV6, and $\Delta u = u_o - u_w$, where u_w is the wind speed within the wake region, and
 718 k is the wake growth rate, which is obtained from $k = 0.4I_u$, with I_u , provided in
 719 Table 2, corresponding to each WT in a certain WD, is utilised. While the wake
 720 diameter, $D_w(x) = D_r + 2kx$, is assumed to expand linearly as a function of the
 721 downstream distance at a rate k .
 722

723 • **Frandsen *et al.* model:**

724 Frandsen *et al.* [12] applied both mass and momentum conservation equations
 725 over a control volume surrounding the turbine to derive their model. Similar to
 726 Jensen model, the top-hat shape was assumed for velocity-deficit profiles in the wake
 727 [5,12,13]. The model is defined as follows:
 728

729
$$\frac{\Delta u}{u_o} = 0.5 \left(1 - \sqrt{1 - \frac{2C_T}{\beta + \alpha\tilde{x}}} \right) \quad (A.2)$$

730 where α is the wake expansion factor, equal to $10k$, while β is function of C_T , and it
 731 is meaningful for values of C_T between 0 and 1 [5,12], which was ensured before
 732 using the model. Additionally, $D_w(x) = D_r(\beta^{1.5} + \alpha\tilde{x})^{\frac{1}{3}}$, and β is expressed by:
 733
 734

735
$$\beta = \frac{1 + \sqrt{1 - C_T}}{\sqrt{1 - C_T}} \quad (A.3)$$

736
 737 • **Bastankhah and Porté-Agel model:**

738 Bastankhah and Porté-Agel [13] developed an extension of Jensen model in which
 739 the linear wake expansion is retained, but the overly simplified top-hat profile is
 740 replaced with a Gaussian self-similar profile, which more closely approximates a
 741 classic far-wake profile [5,13]. It is described by:
 742

743

$$\frac{\Delta u}{u_o} = \left(1 - \sqrt{1 - \frac{C_T}{8(\sigma/D_r)^2}} \right) \exp \left(-0.5 \left[\frac{y^2}{\sigma^2} + \frac{(z - z_h)^2}{\sigma^2} \right] \right)$$

744

745

746

747

748

749

- **Blondel and Cathelain model:**

750

751

752

753

754

755

756

757

758

with $\sigma = k_w x + 0.2\sqrt{\beta}D_r$ the standard deviation of the Gaussian-like velocity deficit profiles at each x as stated in [13], and k_w the wake growth rate for this model taken as $k_w \approx 0.3837I_u + 0.0037$ [5,32,40]. I_u is provided in Table 2.

Blondel and Cathelain model [15] takes into account the near-wake zone, as the absolute Gaussian shape is replaced with a super-Gaussian shape, in addition to preserving the mass and momentum conservation. The super-Gaussian function tends towards a top-hat shape for high values of the super-Gaussian order n in the near-wake conditions, and n decreases gradually with the downstream distance x . This gradual decrease involves a gradual transition in the shape of the wake velocity profiles, from super-Gaussian to Gaussian. Once $n = 2$, the traditional Gaussian shape is recovered, which signifies reaching the far-wake region. It is expressed by:

759

$$\frac{\Delta u}{u_o} = \left(2^{\frac{2}{n}-1} - \sqrt{2^{\frac{4}{n}-2} - \frac{nC_T}{16\Gamma(2/n)\tilde{\sigma}^{4/n}}} \right) \exp \left(-\frac{\tilde{r}^n}{2\tilde{\sigma}^2} \right) \quad (\text{A.5})$$

760

761

762

763

764

765

766

767

768

769

770

771

772

773

774

775

776

777

778

779

780

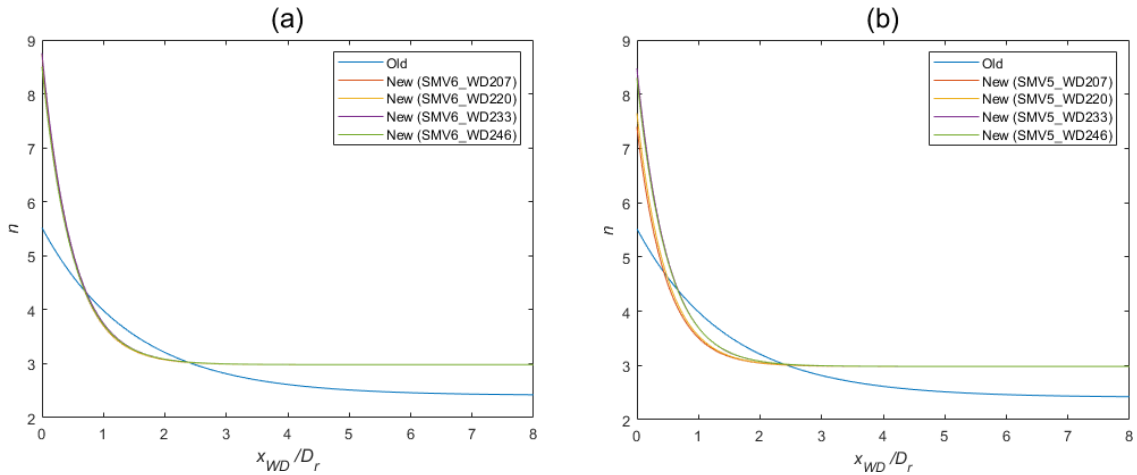
781

782

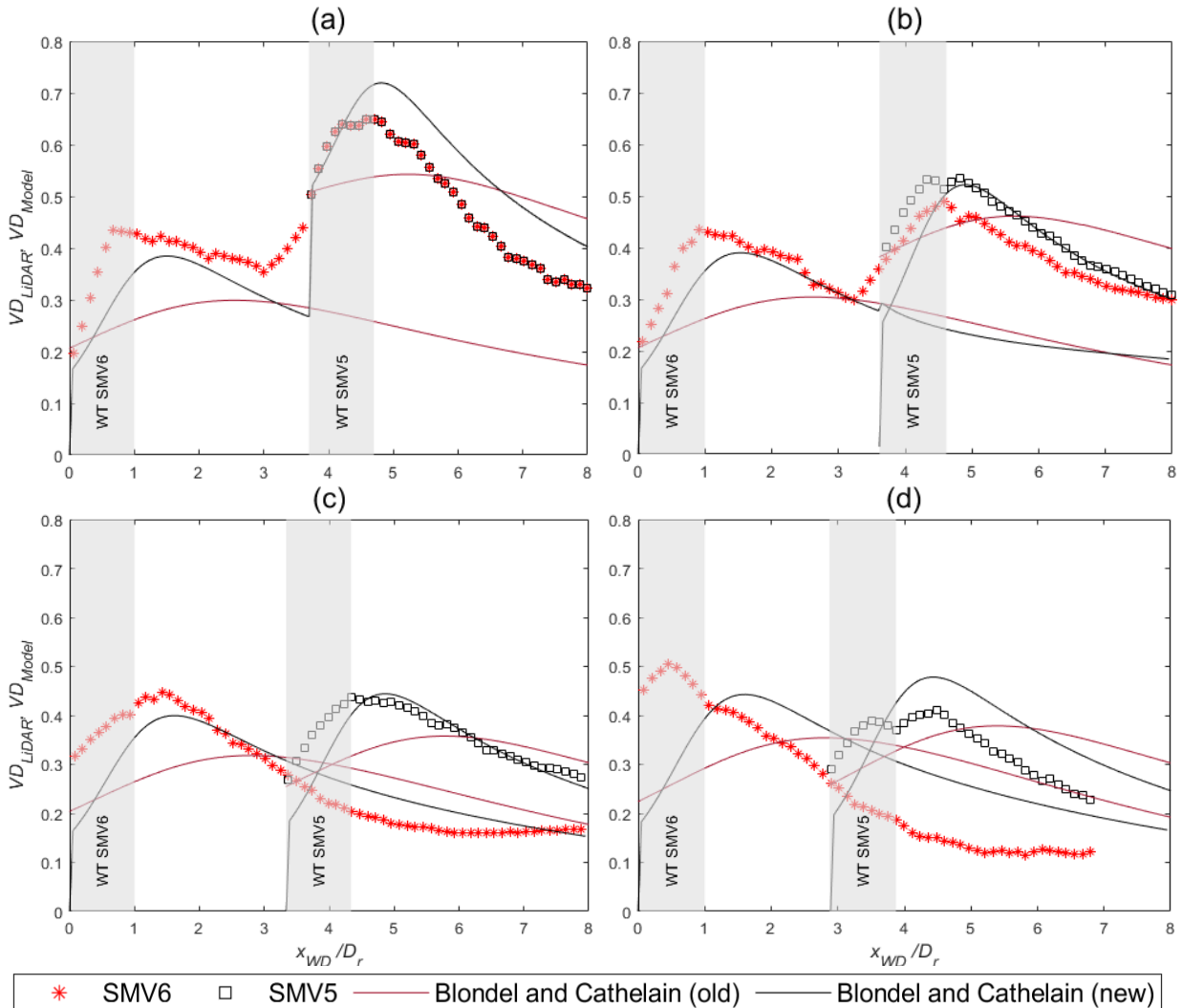
783

where Γ is the Gamma function, while $\tilde{\sigma}$ and \tilde{r} are the standard deviation and the radial distance from the wake centre respectively. The tilde symbol denotes a normalisation by the wind turbine diameter, D_r . The wake characteristic width is $\tilde{\sigma} = (0.17I_u + 0.005)\tilde{x} + 0.2\sqrt{\beta}$ in the original version of the model in [15], but after the further calibration and validation performed in [37], it became $\tilde{\sigma} = (0.18I_u + 0.0119)\tilde{x} + (0.0564C_T + 0.13)\sqrt{\beta}$. Regarding n , it can be obtained using; $n \approx a_f e^{b_f \tilde{x}} + c_f$, with $a_f = -3.11$, $b_f = -0.68$, and $c_f = 2.41$ according to the original model [15], however, after calibration in [37], a_f takes the value which ensures that the maximum normalised velocity deficit at the disk, $VD_{max}(0)$, equals the axial induction factor ($a = 0.5[1 - \sqrt{1 - C_T}]$), $b_f = 1.59e^{-23.31I_u} - 2.15$, and $c_f = 2.98$. This development in the model is explained in both Figs. A.1 & A.2. It fair to say that n differs from one wind farm to another depending on the operating conditions.

Fig. A.1 shows the evolution of n with respect to x/D_r for both versions. It appears that n does not reach 2. Hence, the typical Gaussian shape of the far-wake is not imposed even at $x/D_r = 8$, which is confirmed in Fig. A.2. This is only correct for the old model. For the new model, n does not reach 2 either. However, it produces considerably improved results, and the Gaussian shape is imposed in the far-wake as shown in Fig. A.2. This demonstrates the improvement incorporated in the new model.



784 **Figure A.1:** Evolution of the super-Gaussian order (n) with the normalised downstream distance
 785 (x/D_r) for both the old and new versions of Blondel and Cathelain wake model, with (a) WT-SMV6, (b)
 786 WT-SMV5



787 **Figure A.2:** Comparison between the evolution of the normalised velocity deficits (VD)
 788 calculated at $y = 0$ and the measurement altitude (z), and obtained from both the old and new
 789 versions of Blondel and Cathelain wake model superimposed by Lissaman method (VD_{Model}),
 790 with the one obtained experimentally (VD_{LIDAR}) in the four WDs depicted from Torres-Garcia *et*
 791

792 *al.* [1], with respect to the normalised downstream distance (x/D_r). (a) $WD = 207^\circ$, (b) $WD =$
 793 220° , (c) $WD = 233^\circ$, (d) $WD = 246^\circ$.

794
 795 - **Appendix B: Wake superposition methods**

796 • **Lissaman method:**

797 Lissaman's technique is based on the linear superposition of velocity deficit, and is
 798 defined as in [36]:

$$799 \quad u(X) = u_\infty - \sum_{i=1}^n \Delta u_i(X) \quad (\text{B.1})$$

800 where $\Delta u_i(X) = u_\infty - u_i(X)$.

802 • **Katić *et al.* method:**

803 This technique is based on the linear superposition of energy deficit, and is expressed
 804 as in [38]:
 805

$$806 \quad u(X) = u_\infty - \sqrt{\sum_{i=1}^n \Delta u_i^2(X)} \quad (\text{B.2})$$

807 where $\Delta u_i(X) = u_\infty - u_i(X)$.

809 • **Voutsinas *et al.* method:**

810 Similar to Katić *et al.* method, this technique is based on the linear superposition of
 811 energy deficit, and is given as in [39]:

$$812 \quad u(X) = u_\infty - \sqrt{\sum_{i=1}^n \Delta u_i^2(X)} \quad (\text{B.3})$$

813 where $\Delta u_i(X) = u_{in,i} - u_i(X)$.

815 • **Niayifar and Porté-Agel method:**

816 Similar to Lissaman's method, this method is based on the linear superposition of
 817 velocity deficit, and is given as in [40]:

$$818 \quad u(X) = u_\infty - \sum_{i=1}^n \Delta u_i(X) \quad (\text{B.4})$$

819 where $\Delta u_i(X) = u_{in,i} - u_i(X)$.

820 Although, Lissaman, and Niayifar and Porté-Agel share the same approach, and the same
 821 case applies for Katić *et al.*, and Voutsinas *et al.*, however, there is a difference when it comes to
 822 calculating $\Delta u_i(X)$. As it is calculated based on the undisturbed incoming boundary-layer flow
 823 speed, u_∞ , in case of Lissaman and Katić *et al.*, however, it is calculated using, $u_{in,i}$ the incoming
 824 flow speed for that (*i*th) wind turbine [5] in case of Voutsinas *et al.* and Niayifar and Porté-Agel.
 825 So, the differences in the superposition methods arise from; 1) Different superposition principles;
 826 linear superposition of velocity deficit or energy deficit, 2) Different definitions of the velocity
 827 deficit caused by the *i*th turbine.
 828

829 - **Appendix C: Performance measures**

830 There are two types of errors: systematic error (e.g., uncalibrated sensor), which refers to the
 831 ratio of the model predictions (C_p) to the observations (C_o), and random error, which is due to
 832 unpredictable fluctuations [44]. Each one of the measures indicates one of them, or sometimes
 833 both. Those performance measures are given as follows [44,45]:

- 834 • **Fractional Bias (FB)**: Measures only the mean relative bias indicating the systematic
 835 error of a model that refers to the arithmetic difference between C_p and C_o , and is based
 836 on a linear scale. FB is expressed by:

$$837 \quad FB = \frac{(\overline{C_o} - \overline{C_p})}{0.5(\overline{C_o} + \overline{C_p})} \quad (C.1)$$

- 838 • **Geometric Mean Bias (MG)**: Does the same task as FB, however, the difference
 839 between them is that MG is based on a logarithmic scale, which is more suitable in case
 840 C_p and C_o vary by many orders of magnitude, and it is described by:

$$841 \quad MG = e^{\overline{\ln(C_o)} - \overline{\ln(C_p)}} \quad (C.2)$$

- 843 • **Normalised Mean Squared Error (NMSE)**: A measure of the mean relative scatter
 844 and describes both systematic and random errors. It is based on a linear scale like FB,
 845 and is given by:

$$846 \quad NMSE = \frac{\overline{(C_o - C_p)^2}}{\overline{C_o C_p}} \quad (C.3)$$

- 847 • **Geometric Variance (VG)**: A measure of the mean relative scatter as well as NMSE,
 848 but based on a logarithmic scale, and is given by:

$$849 \quad VG = e^{\overline{(\ln(C_o) - \ln(C_p))^2}} \quad (C.4)$$

- 850 • **Correlation Coefficient (R)**: Demonstrates the linear relationship between two
 851 variables, and expressed by:

$$852 \quad R = \frac{\overline{(C_o - \overline{C_o})(C_p - \overline{C_p})}}{\sigma_{C_o} \sigma_{C_p}} \quad (C.5)$$

- 853 • **The fraction of predictions within a factor of two of observations (FAC2)**: The
 854 most robust measure, because it is not overly influenced by high and low outlier, and it
 855 is described by:

$$856 \quad 0.5 \leq FAC2 = \frac{C_p}{C_o} \leq 2 \quad (C.6)$$

857 where the overbar \overline{C} denotes the average value all over the dataset, and σ_C expresses the standard
 858 deviation all over the dataset.

859

860 - Appendix D: LiDAR measurements altitudes

861

Z_{SMV6}				Z_{SMV5}			
207°	220°	233°	246°	207°	220°	233°	246°
99.11	99.14	99.06	99.01	86.04	85.69	85.71	85.86
98.63	98.58	98.44	98.37	85.63	85.19	85.12	85.23
98.14	98.02	97.82	97.72	85.22	84.68	84.54	84.60
97.67	97.47	97.20	97.08	84.82	84.18	83.96	83.96
97.19	96.91	96.58	96.43	84.41	83.69	83.38	83.33
96.71	96.36	95.97	95.79	84.01	83.20	82.79	82.70
96.24	95.80	95.35	95.14	83.62	82.71	82.21	82.07
95.77	95.25	94.73	94.50	83.23	82.22	81.63	81.44
95.29	94.70	94.12	93.86	82.84	81.73	81.06	80.81
94.83	94.15	93.50	93.21	82.45	81.25	80.48	80.18

94.36	93.59	92.89	92.57	82.06	80.76	79.91	79.55
93.90	93.05	92.27	91.92	81.68	80.28	79.34	78.92
93.44	92.50	91.65	91.28	81.31	79.81	78.77	78.29
92.98	91.96	91.04	90.63	80.93	79.34	78.19	77.66
92.52	91.42	90.42	89.99	80.56	78.87	77.62	77.03
92.07	90.88	89.81	89.34	80.20	78.39	77.05	76.40
91.61	90.33	89.19	88.70	79.84	77.92	76.48	75.78
91.16	89.79	88.58	88.05	79.48	77.45	75.91	75.15
90.72	89.25	87.97	87.41	79.12	76.99	75.35	74.52
90.27	88.71	87.36	86.76	78.77	76.54	74.78	73.90
89.83	88.18	86.75	86.12	78.42	76.08	74.22	73.27
89.39	87.65	86.14	85.47	78.08	75.62	73.66	72.64
88.95	87.12	85.53	84.83	77.74	75.17	73.10	72.02
88.51	86.59	84.92	84.19	77.40	74.72	72.54	71.39
88.08	86.06	84.31	83.54	77.07	74.28	71.98	70.77
87.65	85.53	83.70	82.90	76.74	73.84	71.42	70.14
87.23	85.00	83.09	82.25	76.42	73.40	70.87	69.52
86.80	84.47	82.48	81.61	76.10	72.96	70.31	68.89
86.38	83.95	81.88	80.96	75.79	72.52	69.76	68.27
85.96	83.43	81.27	80.32	75.47	72.10	69.21	67.65
85.55	82.91	80.66	79.67	75.17	71.67	68.66	67.02
85.13	82.40	80.06	79.03	74.86	71.25	68.12	66.40
84.72	81.88	79.45	78.39	74.56	70.83	67.57	65.78
84.32	81.37	78.85	77.74	74.27	70.41	67.03	—
83.91	80.85	78.24	77.10	73.98	70.00	66.49	—
83.51	80.34	77.64	76.45	73.70	69.59	65.96	—
83.11	79.83	77.04	75.81	73.42	69.18	65.42	—
82.71	79.33	76.44	75.16	73.07	68.78	64.88	—
82.32	78.82	75.84	74.52	—	68.38	64.35	—
81.93	78.32	75.24	73.88	—	67.99	63.82	—
81.54	77.82	74.64	73.23	—	67.54	—	—
81.16	77.32	74.04	72.59	—	67.02	—	—
80.78	76.82	73.44	71.94				
80.41	76.33	72.85	71.30				
80.04	75.84	72.25	70.65				
79.67	75.35	71.66	70.01				
79.30	74.87	71.06	69.37				
78.94	74.38	70.47	68.72				
78.58	73.89	69.88	68.08				
78.23	73.42	69.29	67.44				
77.88	72.94	68.70	66.79				
77.53	72.47	68.11	66.15				
77.19	72.00	67.52	65.50				
76.85	71.53	66.93	64.86				
76.52	71.06	66.35	64.22				
76.19	70.60	65.76	63.57				
75.86	70.14	65.18	—				
75.54	69.68	64.60	—				
75.22	69.23	64.02	—				

74.91	68.77	63.44	-
74.60	68.33	62.86	-
74.29	67.89	62.28	-
73.99	67.45	61.71	-
73.69	67.01	61.13	-
73.40	66.57	60.56	-
73.12	66.14	59.99	-
72.83	65.72	59.42	-
72.56	65.29	-	-
-	64.87	-	-
-	64.45	-	-
-	64.04	-	-
-	63.64	-	-
-	63.23	-	-
-	62.83	-	-

862